*photonics*

MDPI

*Article*

# Polarization Calibration and Analysis of Solar-Induced Chlorophyll Fluorescence Wide-Swath Ultraspectral Imaging Spectrometer

**Yiwei Li [1,2], Kaiqin Cao [1], Zongcun Zhang [1], Xiaowei Jia [1], Xuefei Feng [1], Lu Liu [1] and Yinnian Liu [1,2,*]**

[1] Shanghai Institute of Technical Physics, Chinese Academy of Sciences, Shanghai 200083, China; liyiwei21@mails.ucas.ac.cn (Y.L.)
[2] University of Chinese Academy of Sciences, Beijing 100049, China
* Correspondence: ynliu@mail.sitp.ac.cn

**Abstract**

Spaceborne detection of solar-induced chlorophyll fluorescence (SIF) requires extremely high radiometric accuracy, and the polarization characteristics of an ultra-wide swath spaceborne fluorescence ultraspectral camera directly affect the accuracy of SIF retrieval. This study takes an ultra-wide swath camera based on an off-axis three-mirror anastigmat telescope combined with a Littrow–Offner spectrometer as the research object. A full-field-of-view (FOV), full-spectral, pixel-by-pixel polarization testing system was established based on the Stokes–Muller formalism, achieving for the first time fine characterization and calibration of the pixel-level polarization properties of such a payload. The results show that: (1) polarization sensitivity (LPS) exhibits a strong linear positive correlation with wavelength ($R^2 > 0.97$), with good uniformity (fluctuation < 1%) across the full ±15° FOV; (2) the polarization sensitive axis (PSA) shows a symmetric distribution across the FOV and gradually approaches 90° as the wavelength increases, with a clear deviation in the short-wavelength bands and stabilization in the mid-to-long wavelength bands; (3) through multiple sets of cross-validation and Monte Carlo statistics, the calibration accuracy reaches 0.1%, and the system uncertainty is better than 0.05%. This study can provide data support and a reference basis for high-accuracy spaceborne SIF retrieval, payload polarization correction, and optical design optimization.

**Keywords:** solar-induced chlorophyll fluorescence (SIF); ultraspectral imaging spectrometer; polarization response performance; polarization calibration; polarization response characterization

Check for updates

Received: 6 March 2026
Revised: 6 May 2026
Accepted: 12 May 2026
Published: 16 May 2026

**Copyright:** © 2026 by the authors. Licensee MDPI, Basel, Switzerland. This article is an open access article distributed under the terms and conditions of the Creative Commons Attribution (CC BY) license.

## 1. Introduction

Solar-induced chlorophyll fluorescence directly probes vegetation photosynthesis, enabling non-destructive, real-time monitoring of physiological status and productivity. It has become a key indicator for global carbon cycle and agricultural remote sensing [1–9]. However, accurate spaceborne SIF detection faces two major challenges. First, the SIF signal is extremely weak, contributing only 1–2% of the solar reflectance in the 650–800 nm range. Extracting it typically requires $O_2$-A or Fraunhofer lines and ultra-high spectral resolution (<0.3 nm) [9–15]. Second, the optical systems designed to meet these "weak signal, high resolution" requirements often incorporate convex blazed gratings and high-curvature lenses [16–23], which introduce significant polarization sensitivity [24–26]. While laboratory calibration typically uses unpolarized sources, actual top-of-atmosphere (TOA) signals

are strongly polarized by atmospheric and surface scattering [27,28]. The instrument's polarization response thus couples with the input polarization state, corrupting radiometric accuracy and introducing systematic errors into SIF retrieval algorithms. Consequently, systematic characterization of the fluorescence ultraspectral camera's intrinsic polarization response is essential to overcome inversion accuracy limits and fully realize its capability as a photosynthesis probe.

Research on the polarization response of spaceborne remote sensing instruments has established a theoretical and systematic testing methodology centered on the Stokes–Mueller theory. Several studies have revealed the polarization sensitivity data of various payloads through theoretical models and calibrations. For example, the analysis of polarization anomaly signals of general-purpose remote sensors such as MODIS [29–31], and the polarization calibration studies of specialized instruments such as ultraviolet (UV) and multi-angle polarization [32–36], not only enriched the understanding of the polarization characteristics of instruments, but also verified that polarization characterization is a key prerequisite for improving the quality of radiometric data and optimizing optical design [37–39]. Specifically, in the cutting-edge field of chlorophyll fluorescence detection, the studies on the ESA FLEX and China's TECIS are representative [3,40]. Among existing studies, FLEX reported LPS values at a few characteristic wavelengths for three FOV positions (covering $\pm 5.2^{\circ}$), noting that the polarization sensitivity of its optical system without a depolarizer is within 17.4% [41,42]. TECIS conducted a full polarization test over the 670–780 nm wavelength range at three FOV positions (center and edges, covering a total FOV of $4^{\circ}$ [43]), and its LPS without a depolarizer ranges from 1% to 16% across different wavelengths [40]. In both studies, the information on the spatial distribution of LPS is relatively limited. They report LPS values at the center and $\pm 1$ FOV positions, but do not fully elucidate the complete distribution of polarization characteristics across the entire FOV, nor do they investigate the PSA or its distribution patterns. To date, research on the polarization characteristics of fluorescence ultraspectral imagers has revealed mostly localized properties, and the complete polarization characteristics of wide-FOV, large-swath fluorescence imagers in both spatial and spectral dimensions have not yet been fully reported. The self-developed ultra-wide swath spaceborne fluorescence ultraspectral camera used in this study integrates an off-axis three-mirror anastigmat telescope and an integrated optical path Littrow–Offner convex grating spectrometer. It possesses a $\pm 15^{\circ}$ FOV and an ultra-wide swath of 300 km, with a spectral resolution better than 0.3 nm in the 665–780 nm fluorescence spectral region [44]. Table 1 shows the comparison of several performance indicators of typical SIF imagers. It is therefore necessary to clarify the two-dimensional (spatial-spectral) polarization response characteristics to support high-accuracy quantitative retrieval of the extremely weak chlorophyll fluorescence signal.

This paper focuses on the ultra-wide swath spaceborne fluorescence ultraspectral camera, which integrates an off-axis three-mirror anastigmat telescope with a Littrow–Offner configuration spectrometer, and conducts a detailed characterization of its polarization properties across the full field of view (FOV) and full spectral range. A dedicated polarization test platform based on the Stokes–Muller formalism was established, enabling for the first time the acquisition of pixel-level polarization parameters of the camera. The polarization response characteristics across the full wavelength range and full FOV were analyzed, and a quantitative evaluation of the polarization calibration accuracy was completed. The results can provide critical support for precise correction of on-orbit detection data from this payload and complement the current incompleteness in polarization characterization studies of fluorescence detection payloads. Furthermore, the entire set of methods developed in this work can serve as an important theoretical reference and engineering

practical basis for polarization effect management and structural optimization design of future high-performance optical systems with similar configurations.

**Table 1.** Specification comparison: this study's fluorescence ultraspectral camera vs. existing similar payloads.

| Imager | TECIS | FLEX | Proposed Imager |
|---|---|---|---|
| Spectral Range/nm | 670–780 | 677~697, 740~780 | 665~780 |
| Spectral resolution/nm | ≤0.3 | ≤0.3 | ≤0.3 |
| Spatial resolution/m | 370 × 800 | 300 | 240 |
| Swath/km | 34 | ≥150 | 300 |
| Camera polarization sensitivity (LPS) | 1–16% | 8–17.4% | 0.2–8% |
| Polarization calibration accuracy | 0.8% | / | 0.1% |

## 2. Methods and Experiments

### *2.1. Polarization Calibration Model of the Ultraspectral Camera*

The solar-induced fluorescence signal of terrestrial vegetation is very weak, accounting for only 0.5–2% of the total surface signals received by the satellite sensor. During the on-orbit observation of the spaceborne fluorescence ultraspectral camera, in addition to the target fluorescence, a large amount of non-fluorescent stray radiation is also received at the entrance pupil. Studies have shown that the scattered radiation of surface targets such as vegetation canopy, crops, and grasslands has a certain degree of polarization [45]. In addition, the radiation entering the ultraspectral camera is also superimposed with the polarization effect generated by atmospheric scattering. Since the components in the fluorescence optical system respond differently to incident light of different polarization states, the overall system response will change with the incident polarization state. This is described by the polarization sensitivity of the instrument, which is an optical property of the instrument itself. According to the above definition, the polarization sensitivity of the spaceborne fluorescence ultraspectral camera can be expressed as [34]:

$$LPS = \frac{DN_{max} - DN_{min}}{DN_{max} + DN_{min}}. \quad (1)$$

where $DN_{max}$ and $DN_{min}$ are the maximum and minimum values of the system output signal, respectively.

Based on the on-orbit polarization response theory of spaceborne remote sensing instruments [46], the on-orbit output signal of the spaceborne fluorescence ultraspectral camera detector can be modeled as a linear superposition of a dark signal independent of incident radiation and a response signal to radiation at the entrance pupil:

$$DN_{total} = DN_{dark} + DN_{signal} = DN_{dark} + R_{response} \cdot L_{in}. \quad (2)$$

For a spaceborne fluorescence ultraspectral camera, its optics comprise an off-axis TMA telescope and a Littrow–Offner ultraspectral spectrometer sharing a convex grating path. According to Knight's theory, their polarization responses are described by Mueller matrices $M_{\mathrm{TMA}}$ and $M_{\mathrm{spec}}$. The incident light at the entrance pupil is represented by Stokes parameters [47]. In spaceborne Earth remote sensing, the circular polarization component of the TOA radiation is typically negligible [48]. Thus, polarization state at the entrance pupil simplifies to a Stokes vector:

$$L_{in} = [I_{\mathrm{in}}\ Q_{\mathrm{in}}\ U_{\mathrm{in}}\ 0]^{\mathrm{T}}. \quad (3)$$

where $I_{\text{in}}$ represents the total radiance at the entrance pupil, and $Q_{\text{in}}$, $U_{\text{in}}$, and $V_{\text{in}}$ are the $P_H - P_V$, $P_{45} - P_{135}$ and $P_R - P_L$ components of the incident light, respectively. After this radiation is transmitted sequentially through the telescope, ultraspectral spectrometer, and other optical systems, its exit Stokes vector can be obtained by multiplying the incident vector by the overall Mueller matrix of the system. Considering the detector's dark signal and photoelectric conversion response, the total signal output by the detector can be modeled as:

$$D_{\text{total}} = D_{\text{dark}} + D_{\text{signal}} = D_{\text{dark}} + R_{\text{detector}} M_{\text{spec}} M_{\text{TMA}} L_{\text{in}}. \quad (4)$$

Based on the assumption that the detector is polarization independent, the signal term in Equation (4) can be simplified to the detector's response to the total intensity of the outgoing light only, from which the following can be derived:

$$D_{\text{signal}} = [R_D\ 0\ 0\ 0] I_{\text{in}} \begin{bmatrix} m_{11} & \cdots & m_{14} \\ \vdots & \ddots & \vdots \\ m_{41} & \cdots & m_{44} \end{bmatrix} \begin{bmatrix} 1 \\ \frac{Q_{\text{in}}}{I_{\text{in}}} \\ \frac{U_{\text{in}}}{I_{\text{in}}} \\ 0 \end{bmatrix} = R_D I_{\text{in}} \left( m_{11} + m_{12} \frac{Q_{\text{in}}}{I_{\text{in}}} + m_{13} \frac{U_{\text{in}}}{I_{\text{in}}} \right). \quad (5)$$

In this formula, $M = M_{\text{spec}} M_{\text{TMA}}$ is the Mueller matrix of the spaceborne fluorescence ultraspectral camera, with elements $m_{ij} (i, j = 1, 2, 3, 4)$, and $R_D$ is the polarization-independent response factor that integrates the detector and electronic responses. This formula quantitatively reveals the physical nature of the instrument's polarization sensitivity—when the incident light has polarization characteristics and the instrument's optical system is sensitive to polarization, a polarization-related error term is generated, which is added to the ideal response. The more pronounced the polarization of the incident light and the stronger the instrument's polarization response, the greater the detection error introduced by polarization.

According to Knight's polarization calibration theory, during the prototype development stage, as long as the incident light with a known polarization state is used for polarization testing, the Mueller matrix of the instrument can be obtained through the output signal of the instrument, thereby realizing the polarization calibration of the instrument. For linearly polarized incident light, the behavior of its Stokes vector can be expressed as [49]:

$$S_{\text{in}} = I_{\text{in}} \cdot [1\ \cos 2\beta\ \sin 2\beta\ 0]^{\text{T}}. \quad (6)$$

At this point, $S_{in}$ describes linearly polarized light measured counterclockwise from the x-reference axis, with a direction angle of β and a degree of polarization of 1. Now, we focus on the effective signal excluding the dark signal; the output Stokes vector for this portion of the optical signal is:

$$D = R_D \cdot I_{\text{in}} \cdot (m_{11} + m_{12} \cos 2\beta + m_{13} \sin 2\beta) = R_D \cdot I_{\text{in}} \cdot m_{11} \cdot (1 + m_2 \cos 2\beta + m_3 \sin 2\beta). \quad (7)$$

where $m_2 = \frac{m_{12}}{m_{11}}$, $m_3 = \frac{m_{13}}{m_{11}}$ are the normalized Mueller matrix elements of the spaceborne fluorescence ultraspectral camera, which can characterize the polarization response characteristics of the camera as a whole. $\beta$ is the polarization azimuthal angle describing the polarization orientation of linearly polarized light. According to the definition of polarization sensitivity, the polarization sensitivity of the spaceborne fluorescence ultraspectral camera satisfies:

$$LPS = \frac{S_{\text{signal|max}} - S_{\text{signal|min}}}{S_{\text{signal|max}} + S_{\text{signal|min}}} = \frac{(R_{\text{N}} I_{\text{in}} m_{11}) \left[ 1 + \sqrt{m_2^2 + m_3^2} - \left( 1 - \sqrt{m_2^2 + m_3^2} \right) \right]}{(R_{\text{N}} I_{\text{in}} m_{11}) \left[ 1 + \sqrt{\text{m}_2^2 + m_3^2} + \left( 1 - \sqrt{\text{m}_2^2 + m_3^2} \right) \right]} = \sqrt{m_2^2 + m_3^2}. \quad (8)$$

Substituting *LPS* into Equation (8) yields:

$$D_{\text{signal}} = \mathrm{R_D}\cdot I_{\text{in}}\cdot m_{11} + R_D\cdot I_{\text{in}}\cdot m_{11}\cdot LPS\cdot\cos(2\beta - 2\varphi). \quad (9)$$

$R_D$ is the detector responsivity, $I_{\text{in}}$ is the radiance at the entrance pupil, $\beta$ is the polarization azimuth angle of the incident polarized light, *LPS* is the polarization sensitivity of the optical system, and $\varphi$ is the direction of the camera's polarization sensitive axis (PSA). Based on the above mechanism, using a linearly polarized light source with good linearity as the input light signal, a one-to-one mapping is established between the polarization sensitivity $LPS_{(\mathrm{Ch,Col})}$, the polarization sensitive axis $\varphi_{(\mathrm{Ch,Col})}$, and the incident light $(L_{in}, \beta)$ with different polarization states of the fluorescence ultraspectral camera, thus obtaining the polarization response characteristics of the spaceborne fluorescence ultraspectral camera. Here Ch in parentheses represents the channel number of the pixel's band, and Col represents the column number of the pixel's FOV.

### *2.2. Polarization Response Testing of the Fluorescence Ultraspectral Camera*

In this study, a polarization response measurement system was independently built, and the polarization response of the ultraspectral camera under test was characterized using the polarized light source method. The measurement system mainly consists of a polarized light generating module and the ultraspectral camera under test. Its core components include a compact high-brightness integrating sphere, a Thorlabs WP25M-UB1 wire-grid polarizer, a PRM1Z8 rotation mount, a Φ350 mm collimating lens, and a high-precision two-axis rotation stage. During the experiments, the compact high-brightness integrating sphere was used to simulate natural light. The PRM1Z8 rotation mount drove the wire-grid polarizer to continuously generate linearly polarized light over a 0–360° azimuth range. The extinction ratio of the wire-grid polarizer is better than 650:1 at 650 nm, better than 700:1 at 800 nm. The integrating sphere and the polarizer were fixed relative to each other, together forming the polarized light generation module. After beam expansion and collimation, a uniform polarized light beam with a diameter of Φ350 mm was produced, which fully covers the full aperture of the camera. The camera under test operates in the wavelength range of 665–780 nm, with a total of 1380 spectral channels, and its cross-track field of view (FOV) is ±15°, corresponding to 800 detector pixel columns. During the measurement, the light source illuminated approximately 50 FOV columns across the full aperture of the camera. A high-precision two-axis rotation stage was used to accurately switch between different FOVs. The selected central FOV column indices were: Col.100, Col.140, Col.175, Col.220, Col.275, Col.325, Col.375, Col.425, Col.470, Col.525, Col.560, Col.625, Col.645, and Col.700 (out of a total of 800 columns). All measurements were carried out in a darkroom environment. To ensure measurement accuracy, the polarization azimuth angle of the polarizer was precisely controlled by an electronic system with an angular resolution on the order of arcminutes. Data were acquired every 10° from 0° to 360°, with 110 frames collected per data set, and three repeated tests were performed for each region. In addition, both the camera and the light source were powered through the UPS system with built-in power filters, and an oscilloscope was used to monitor the output stability of the constant-voltage power supply of the integrating sphere, further reducing the influence of power supply disturbances on measurement accuracy. During the test, the camera was temperature-controlled using water cooling, and the detector signal was strictly maintained within the linear range (nonlinearity better than 0.95%), significantly reducing systematic errors caused by temperature drift and nonlinearity. The test setup and flow chart are shown in Figure 1.

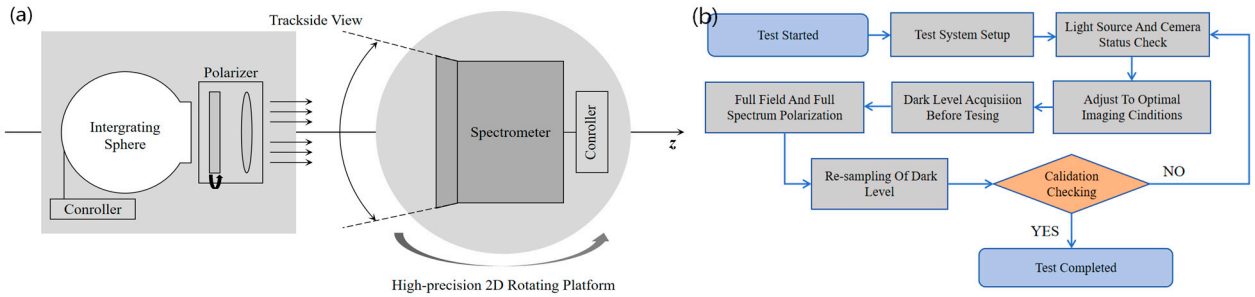



**Figure 1.** (**a**) Schematic diagram of polarization response test of spaceborne fluorescence ultraspectral camera. (**b**) Schematic diagram of spaceborne fluorescence ultraspectral testing system and testing process.

### *2.3. Method for Calibrating and Determining LPS and PSA*

In the polarization calibration experiment, the system sequentially acquires detector response signals at 37 different polarizer angles, with an interval of 10° over the range of 0° to 360°, forming an observation dataset covering a full polarization cycle. Using this set of measured response data as input samples and based on the polarization transfer response model expressed in Equation (10), a polarization response observation equation is established for each spectral channel (Ch) and each pixel column (Col). Since the number of observation equations exceeds the number of unknown parameters (LPS and PSA), the model constitutes an overdetermined system of equations. A least-squares fitting method is then applied to obtain the optimal parameter solution. By solving independently for each element (pixel column) and each spectral channel, the linear polarization sensitivity (LPS) and polarization sensitive axis (PSA) across the full field of view (FOV) and all spectral channels are finally obtained, completing the polarization calibration solution for the system.

$$D_{\text{signal(Ch,Col)}} = \mathrm{R_D}\cdot I_{\text{in}}\cdot m_{11} + R_D\cdot I_{\text{in}}\cdot m_{11}\cdot LPS_{\text{(Ch,Col)}}\cdot\cos\left(2\beta - 2PSA_{\text{(Ch,Col)}}\right) \quad (10)$$

$D_{\text{signal(Ch,Col)}}$ is the detector output response for the Ch-th spectral channel and the Col-th pixel column; where $R_D$ is the detector responsivity, $I_{in}$ is the radiance at the entrance pupil, β is the polarization azimuth angle of the incident polarized light, and $LPS_{(Ch,Col)}$ and $PSA_{(Ch,Col)}$ are the LPS and PSA parameters of the optical system to be calibrated.

### *2.4. Calibration Accuracy Evaluation Method*

To comprehensively and rigorously validate the confidence level of the polarization calibration results, this section quantitatively evaluates both the calibration accuracy and the calibration stability as follows:

(1) Through multiple sets of parallel calibration experiments combined with independent validation, cross-validation of the calibration results and assessment of the calibration accuracy are achieved;
(2) Using Monte Carlo random sampling statistics and the dispersion and convergence behavior of subsets with 18 to 34 sampling points, the stability and system uncertainty of the calibration results obtained from the full set of 37 points are verified.

These two approaches support each other from the perspectives of accuracy and stability, thereby sufficiently demonstrating the reliability of the calibration results.

#### 2.4.1. Calibration Accuracy Validation Using Independent Repeated Measurements

This method uses three sets of parallel calibration experiments and one set of independent validation experiments to verify the calibration accuracy. All experiments are

performed under identical conditions, including equipment parameters and environment, to ensure the comparability of the results.

Among them, Groups 1, 2, and 3 are the parallel calibration groups. Following the calibration procedure described in Section 2.3 of this paper, response data at 37 polarizer angles with a step size of 10° over the range of 0° to 360° were acquired. Three sets of calibration results ($LPS_{i(1,2,3)}$ and $PSA_{i(1,2,3)}$) were independently calculated, and the average $LPS_{mean}$and$PSA_{mean}$ of the three sets was taken as the final calibration output.

Group 4 serves as the independent validation group: it is not involved in the calibration solving process. Instead, the maximum and minimum response signals are obtained by rotating the polarizer through a full cycle, and a validation value $LPS_{verify}$ is directly calculated based on the physical definition of LPS. This validation value is then used to perform an independent accuracy check of the calibration results.

The calibration accuracy of LPS is evaluated using the absolute error:

$$LPS_{Ab_Err} = LPS_{verify} - LPS_{mean} \tag{11}$$

Since there is no external independent true value available for direct validation of the PSA, its stability is evaluated using the maximum absolute deviation of the three calibration results from their mean.

$$PSA_{Ab_Err} = MAX\{PSA_i - PSA_{mean}\} \tag{12}$$

2.4.2. Calibration Uncertainty Analysis Using Monte Carlo Sampling

To verify the statistical stability and system uncertainty of the LPS calibration results, this section takes the complete 37-point calibration dataset as the full set, constructs subsets of varying sizes at equal intervals within the range of 18 to 34 points and performs 10,000 independent random samplings without replacement. Each sampling independently retrieves the LPS, thereby generating a large-sample statistical sequence.

Suppose that under a fixed number of sampling points, $N$ independent LPS retrieval results are obtained. By arranging the sample values in ascending order, we obtain an ordered sequence of $LPS$ samples:

$$LPS_1 \le LPS_2 \le \cdots \ldots \le LPS_N, N = 10{,}000 \tag{13}$$

To characterize the dispersion of the LPS calibration results, this section jointly evaluates the dispersion and stability of the LPS using three types of statistical metrics: the interquartile range (IQR), the 3σ confidence interval, and the extreme range (Max–Min). Based on these, the level of system uncertainty is comprehensively determined.

The position of the quartile is defined as:

$$\begin{cases} P_{OSQ_1 = \frac{N+1}{4}} \\ P_{OSQ_3 = \frac{3(N+1)}{4}} \end{cases} \tag{14}$$

where $P_{OS_{Q1}}$ is the lower quartile position of the LPS samples, and $P_{OS_{Q3}}$ is the upper quartile position of the LPS samples.

$$IQR = Q_3 - Q_1 \tag{15}$$

$Q_3, Q_1$ are the quantile values of the ordered LPS samples at cumulative probabilities of 75% and 25%, respectively. The IQR reflects the dispersion range of the central 50% of the core LPS data.

Arithmetic mean of the LPS samples:

$$\overline{LPS} = \frac{1}{N}\sum_{i=1}^{N} LPS_i \tag{16}$$

Sample standard deviation of the LPS samples:

$$\sigma = \sqrt{\frac{1}{N-1}\sum_{i=1}^{N}\left(LPS_i - \overline{LPS}\right)^2} \tag{17}$$

3σ confidence interval of the LPS calibration results:

$$U_{3\sigma} = \left[\overline{LPS} - 3\sigma, \overline{LPS} + 3\sigma\right] \tag{18}$$

This interval covers 99.73% of the valid LPS retrieval data and reflects the global steady-state fluctuation boundary of the LPS calibration results under random disturbances. It is used to quantitatively evaluate the dispersion and convergence characteristics of LPS under different numbers of sampling points, and to reasonably extrapolate the stability and system uncertainty level of the full 37-point full-angle calibration results.

## 3. Results

### *3.1. Raw Polarization Test Results of the Camera*

Following the test system and method described above, the polarization response characteristics of the spaceborne ultraspectral camera under linearly polarized light incident at polarizer angles from 0° to 360° were measured across the full field of view (FOV) and full spectral range. The response results for different spectral channels and different FOV positions under linearly polarized light incident at various polarizer angles are shown in the following figure:

Figure 2 presents the normalized polarization response raw data curves for different spectral channels and pixel FOV over the 665–780 nm range (blue, red, and yellow lines respectively correspond to spectral channels 18, 706, and 1376). The curves exhibit a distinct dual-period pattern, aligning well with the theoretical model. To further conduct a quantitative study of its described polarization characteristics, polarization calibration and characteristic analysis were performed in both spatial and spectral dimensions.

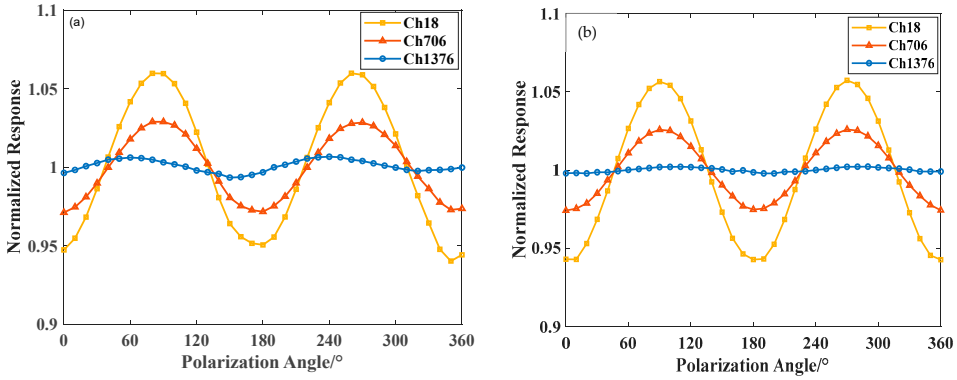



**Figure 2.** Normalized polarization response raw data for different spectral channels: (**a**) Col.100, (**b**) Col.425. "Ch" denotes the spectral channel index, while "Col" indicates the pixel column index.

### *3.2. Polarization Response Calibration of the Camera*

Based on the response signals obtained from testing at 37 polarization angles with a step size of 10 within the range of 0–360 degrees, the calibration results $LPS_{(Ch,Col)}$ and $PSA_{(Ch,Col)}$ for the Ch-th spectral channel and Col-th pixel row were derived according

to the method described in Section 2.3. Table 2 presents the coefficients $LPS_{(Ch,Col)}$ and $PSA_{(Ch,Col)}$ of the polarization response calibration functions for typical field-of-view and band pixels, while Figure 3 shows the response values and polarization fitting curves for these pixels.

**Table 2.** LPS and PSA values of the spaceborne fluorescence ultraspectral camera.

| Cross-Track FOV (Column) | LPS% | | | PSA° | | |
|---|---|---|---|---|---|---|
| | 665 nm | 723 nm | 780 nm | 665 nm | 723 nm | 780 nm |
| 100 | 0.59 | 3.28 | 6.48 | 62.78° | 86.62° | 83.87° |
| 140 | 0.57 | 3.51 | 7.18 | 68.32° | 87.13° | 83.76° |
| 175 | 0.50 | 3.14 | 6.31 | 62.91° | 87.49° | 84.86° |
| 220 | 0.36 | 3.31 | 6.81 | 66.98° | 89.36° | 87.35° |
| 275 | 0.38 | 3.14 | 6.19 | 77.62° | 89.52° | 87.62° |
| 325 | 0.43 | 3.10 | 5.95 | 79.41° | 89.62° | 88.30° |
| 374 | 0.24 | 3.10 | 6.03 | 91.36° | 91.03° | 88.95° |
| 425 | 0.25 | 2.97 | 6.05 | 106.06° | 93.07° | 91.38° |
| 470 | 0.34 | 3.40 | 6.69 | 104.49° | 92.79° | 91.60° |
| 525 | 0.33 | 3.37 | 6.65 | 106.52° | 93.08° | 92.00° |
| 560 | 0.44 | 3.46 | 6.75 | 113.76° | 95.79° | 93.69° |
| 625 | 0.60 | 3.34 | 6.38 | 109.68° | 94.88° | 94.49° |
| 645 | 0.61 | 3.55 | 7.19 | 101.36° | 92.49° | 92.88° |
| 700 | 0.62 | 3.40 | 6.51 | 111.74° | 95.41° | 95.05° |

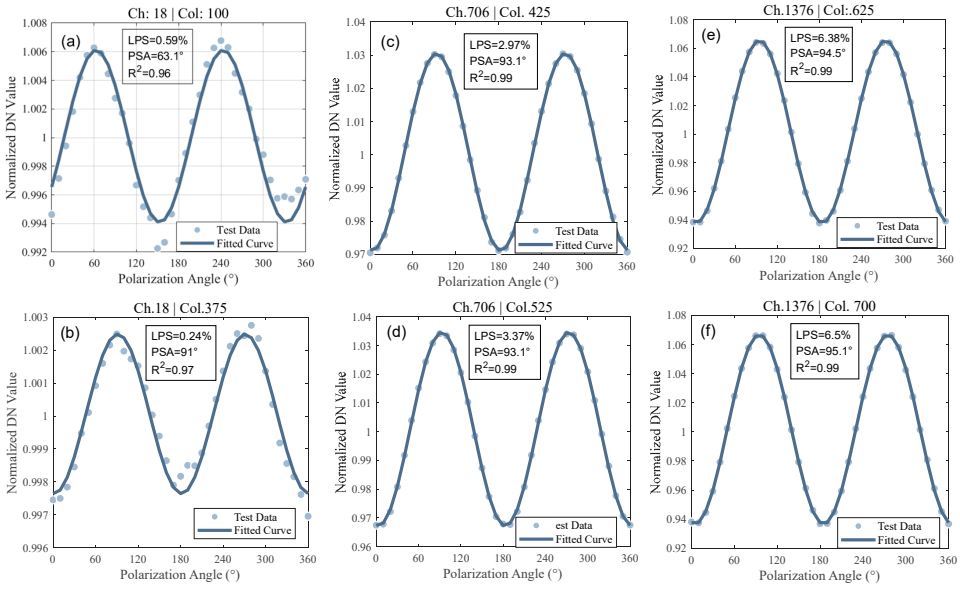



**Figure 3.** Polarization calibration results for different pixels: (**a**) Ch.18-Col.100, (**b**) Ch.18-Col.375, (**c**) Ch.706-Col.425, (**d**) Ch.706-Col.525, (**e**) Ch.1376-Col.625, (**f**) Ch.1376-Col.700. Here, the gray points represent the test data, and the blue solid line represents the fitted curve. "Ch" is the spectral channel number, and "Col" is the pixel column number.

### *3.3. Polarization Response Analysis of Spaceborne Fluorescence Ultraspectral Camera*

#### 3.3.1. Variation in Polarization Sensitivity (LPS) with Wavelength and Cross-Track FOV

Figure 4a shows the distribution of the LPS of the spaceborne fluorescence ultraspectral camera across the full wavelength range and the full field of view (FOV). Figure 4b,c present more detailed trends of LPS variations in the spatial and spectral dimensions, respectively. The data indicate that LPS exhibits a strong wavelength dependence, increasing approximately linearly with wavelength, and the linearity remains largely consistent across different FOVs. The distribution of LPS across the cross-track FOV is relatively smooth

and symmetric, with slightly lower values at the central FOV than at the edges. At 665 nm, the mean LPS across the full FOV is approximately 0.45%, with a range of 0.24–0.62%; at 723 nm, the mean value is about 3.3%, ranging from 2.97% to 3.55%; and at 780 nm, the mean value is about 6.5%, ranging from 5.95% to 7.2%. The distributions in both the spatial and spectral dimensions indicate that the LPS of the camera exhibits good uniformity across a wide FOV of ±15°.

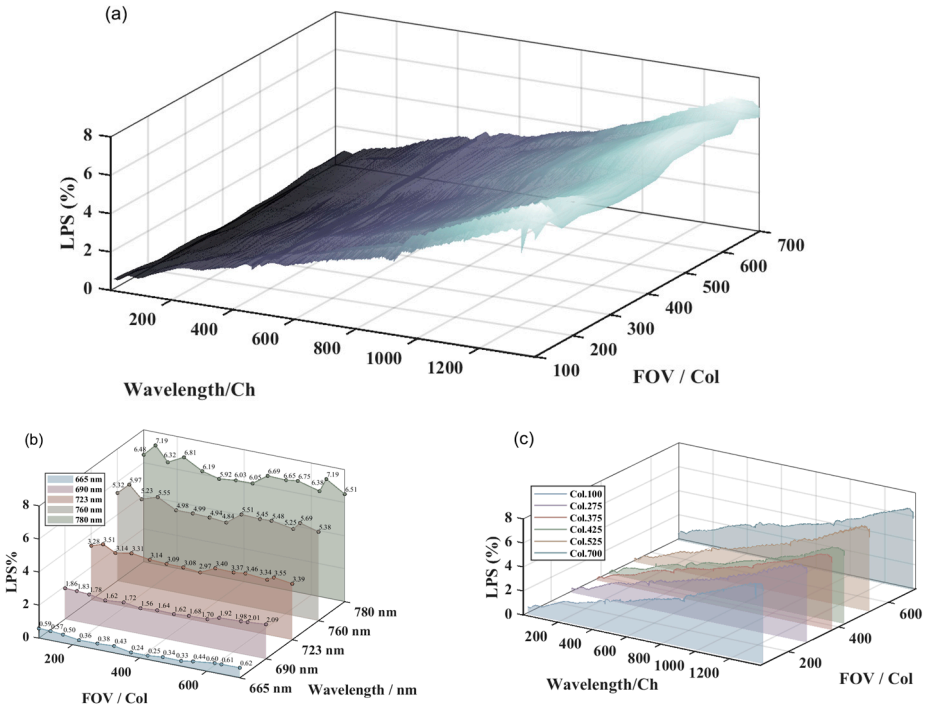



**Figure 4.** (**a**) Two-dimensional (spatial-spectral) distribution of the LPS of the spaceborne fluorescence ultraspectral camera, (**b**) variation in LPS with cross-track field of view (FOV), (**c**) variation in LPS with spectral channel. "Ch" is the spectral channel number, and "Col" is the pixel column number.

### 3.3.2. Variation in Polarization Sensitive Axis (PSA) with Wavelength and Cross-Track FOV

The distribution of the polarization sensitive axis (PSA) is influenced by both wavelength and the cross-track field of view (FOV). Figure 5a shows the distribution of the PSA of the spaceborne fluorescence ultraspectral camera across the full wavelength range and the full field of view (FOV). Figure 5b,c present more detailed trends of PSA variations in the spatial and spectral dimensions, respectively. As the wavelength increases, the PSA of the FOV converges toward 90°. Meanwhile, the variation in PSA with the cross-track FOV exhibits a center-symmetric characteristic, although the behavior differs across wavelengths: at 723 nm and 780 nm, the PSA is mainly distributed in the range of 84° to 95°, showing a gently increasing trend with FOV. At 665 nm, a notably different behavior is observed: the PSA varies over a wider range, approximately 62° to 114°, with a rapid change near the central FOV and a gradual change near the edge FOV. The full-FOV mean PSA values at the three wavelengths are 90.21°, 91.3°, and 89.74°, respectively, all close to 90°. For FOV positions symmetric about the central FOV, the PSA values are approximately complementary.

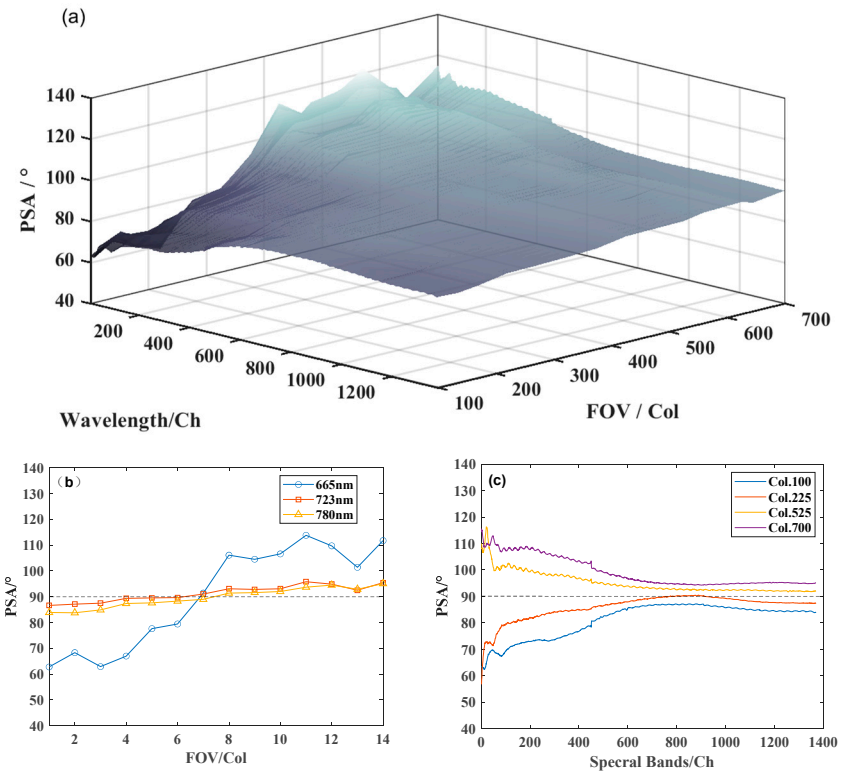



**Figure 5.** (**a**) Spatial-spectral distribution characteristics of the PSA of the spaceborne fluorescence ultraspectral camera, (**b**) variation in PSA with cross-track field of view (FOV), (**c**) variation in PSA with wavelength. "Ch" is the spectral channel number, and "Col" is the pixel column number.

### *3.4. Calibration Accuracy and Uncertainty Results*

#### 3.4.1. Results of Independent Repeated Test Accuracy

Quantitative evaluation of the calibration accuracy of LPS and PSA was conducted through three sets of independent calibration experiments and one set of independent validation experiments. The distribution of absolute errors is shown in Figure 6. Table 3 presents the LPS and PSA calibration results and their mean values from the three independent tests for the central FOV pixel (Col.425) and the edge FOV pixel (Col.625) at three characteristic wavelengths (665 nm, 723 nm, and 780 nm).

**Table 3.** Comparison of calibration results among three independent test sets.

| | **Col.625** | | | | | | **Col.425** | | | | | |
|---|---|---|---|---|---|---|---|---|---|---|---|---|
| | **Group1** | | **Group2** | | **Group3** | | **Group1** | | **Group2** | | **Group3** | |
| Item | LPS/% | PSA/° | LPS/% | PSA/° | LPS/% | PSA/° | LPS/% | PSA/° | LPS/% | PSA/° | LPS/% | PSA/° |
| 665 nm | 0.601 | 110.35 | 0.594 | 109.09 | 0.591 | 109.65 | 0.248 | 105.35 | 0.246 | 105.71 | 0.254 | 106.37 |
| 723 nm | 3.336 | 94.89 | 3.342 | 94.88 | 3.340 | 94.87 | 2.969 | 93.06 | 2.973 | 93.081 | 2.976 | 93.068 |
| 780 nm | 6.378 | 94.50 | 6.377 | 94.50 | 6.379 | 94.48 | 6.043 | 91.37 | 6.042 | 91.39 | 6.04 | 91.36 |

As can be seen from Figure 6 and Table 3, at the three characteristic wavelengths for the central FOV pixel (Col.425) and the edge FOV pixel (Col.625), the absolute errors of LPS are all better than ±0.1%, indicating a calibration accuracy of 0.1%. The three sets of calibration results show high consistency and small differences. Furthermore, it can also be observed that the maximum absolute error of PSA from the three calibrations is better than ±1°.

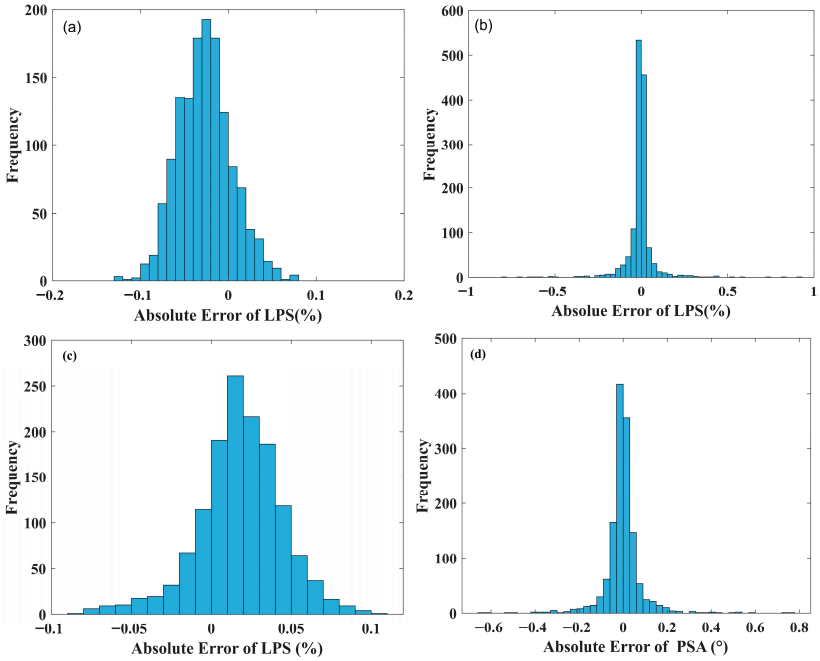



**Figure 6.** Results of absolute errors of polarization calibration: (**a**) absolute calibration error of LPS for pixel Col.425 (%), (**b**) absolute calibration error of PSA (°) for pixel Col.425, (**c**) absolute calibration error of LPS for pixel Col.625 (%), (**d**) absolute calibration error of PSA (°) for pixel Col.625. "Ch" is the spectral channel number, and "Col" is the pixel column number.

### 3.4.2. Monte Carlo Sampling-Based Calibration Uncertainty Results

Figure 7 shows the LPS distribution and convergence trend for the central FOV pixel (Col.425) and the edge FOV pixel (Col.625) at three wavelengths (665 nm, 723 nm, and 780 nm), with the number of sample points ranging from 18 to 34.

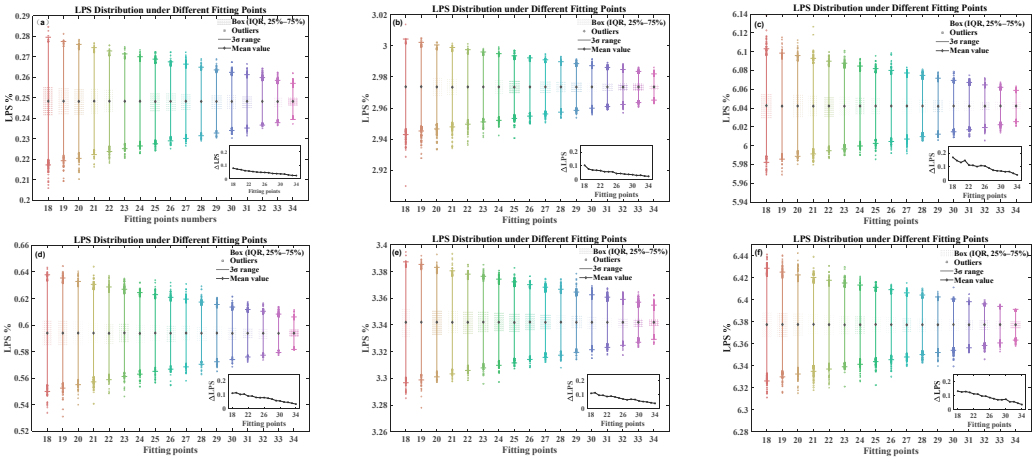



**Figure 7.** LPS calibration results for different numbers of polarizer angles (i.e., different numbers of sampling points): (**a**) Ch.18-Col.425, (**b**) Ch.706-Col.425, (**c**) Ch.1376-Col.425, (**d**) Ch.18-Col.625, (**e**) Ch.706-Col.625, (**f**) Ch.1376-Col.625. "Ch" denotes the spectral channel number, and "Col" denotes the pixel column number. The main panel shows boxplots of the LPS results corresponding to different numbers of sampling points (18, 20, 22, ⋯, 34 points), with the interquartile range and outliers marked, and the 3σ confidence interval error bars overlaid. The inset subplot in the lower right corner shows the trend of the range (maximum minus minimum) of the LPS results as a function of the number of sampling points. In the figure, the box represents the interquartile range (25–75%), the error bars represent the 3σ confidence interval, and the inset curve shows the variation trend of the extreme range of the LPS results under different numbers of sampling points. "Ch" is the spectral channel number, and "Col" is the pixel column number.

As can be seen from the results shown in Figure 7, as the number of sample points increases from 18 to 34, the LPS distribution for the Col.425 and Col.625 pixels shows a clear convergence trend. The 3σ confidence interval gradually narrows to within 0.05%, and the extreme range (max–min) decreases to below 0.1%, resulting in a final system uncertainty better than 0.05%. These results indicate that the proposed polarization calibration method achieves high accuracy, high stability, and high reliability for both the central and edge FOVs. Under the sampling condition with a 10° step, the calibration accuracy and uncertainty metrics can meet the polarization calibration requirements of a spaceborne SIF ultraspectral camera.

## 4. Discussion

This study aims to characterize the polarization response of the spaceborne fluorescence ultraspectral camera, providing support for payload polarization suppression and improving the accuracy of space-based fluorescence detection. A high-precision polarization testing system was established, and full-field-of-view (FOV), full-spectral-range calibration experiments were conducted. The results systematically reveal the polarization distribution of the camera in the spectral and spatial dimensions, and the calibration accuracy is presented.

### *4.1. Spectral–Spatial Correlation Distribution of LPS*

This study indicates that the camera exhibits a clear two-cycle polarization response characteristic to linearly polarized incident light across polarization angles from 0° to 360°. The LPS shows a significant positive correlation with wavelength, with a linear correlation exceeding 97%. This distribution characteristic may be highly related to the polarization properties of the convex grating, which is the key dispersive element of the optical system. Due to its unique geometric microstructure, the convex blazed grating exhibits marked differences in diffraction efficiency between the direction parallel to the grooves and the direction perpendicular to the grooves, thereby inducing a wavelength-dependent polarization effect [16–21].

In terms of spatial distribution, the LPS of the camera varies only slightly (within <1%) across the ±15° cross-track field of view (FOV), exhibiting good uniformity. This differs from the typical behavior observed in other existing fluorescence detection remote sensors, where LPS tends to increase significantly with FOV [47]. This result may be attributed to the combined effect of the optical design of the ultra-wide swath off-axis three-mirror anastigmat telescope—which controls the incident angles on each mirror within the ±15° FOV—and the overall depolarizing coating design of the system. Although a slight increasing trend in LPS is still observed at the edges of the FOV, overall, the consistency of the LPS across the full FOV of the camera is good.

### *4.2. Spectral–Spatial Distribution Characteristics of PSA*

The polarization sensitive axis (PSA) exhibits clear trends in both the wavelength and FOV dimensions: as the wavelength increases, the PSA gradually converges toward 90°; as the cross-track FOV varies, the PSA shows a symmetric distribution centered at 90°. In the mid-to-long wavelength bands (723 nm and 780 nm), the PSA remains stable near 90° (ranging from 84° to 95°), with small fluctuations and good symmetry. In the short-wavelength band (665 nm), the variation range of the PSA expands significantly (from approximately 62° to 114°), and the standard deviation is much larger than that in the longer-wavelength bands. These differences among wavelength bands are hypothesized to be related to the varying relative contributions of the telescope's polarization response and the grating's polarization effects as a function of wavelength. In the longer-wavelength

bands, the polarization effect of the grating is relatively dominant, leading to a more stable distribution. In the shorter-wavelength band, the grating effect weakens, and the geometric phase delay introduced by the telescope across the FOV becomes more influential, ultimately resulting in the observed band-dependent distribution differences.

### *4.3. Stability and Reliability of Calibration Results*

The stability and reliability of the calibration results were evaluated through a combination of Monte Carlo random sampling experiments and multiple sets of parallel repeated tests. Using equally spaced gradient fitting points as a variable, along with descriptive statistical analysis, interval estimation, and mechanism discrepancy analysis, the calibration uncertainty was determined to be 0.05%. A cross-validation strategy based on multiple sets of experimental data, combined with averaging of polarization parameters from three sets of samples and comparison with independent data parameters, demonstrates that under the calibration procedure described in this study, experimental errors caused by external factors such as equipment response fluctuations, minor environmental disturbances, and operational differences are controllable. The calibration accuracy of LPS reaches 0.1%, and that of PSA reaches 1°. The above results are consistent with one another and serve as mutual corroboration and complementation.

## 5. Conclusions

This study focuses on an ultra-wide swath spaceborne fluorescence ultraspectral camera. Based on the Stokes–Muller formalism, a full-field-of-view (FOV), full-wavelength testing system was established, enabling pixel-level, high-precision, and detailed characterization of the polarization properties. The results show that the camera's LPS exhibits a linear positive correlation with wavelength and good uniformity across a ±15° FOV. The PSA gradually approaches 90° as the wavelength increases and shows a symmetric distribution as the FOV expands. The calibration of the polarization parameters in this study has been validated through repeated tests and Monte Carlo simulations, demonstrating high stability and reliability. These findings can provide a core basis for payload polarization correction and operational applications. In the future, based on the detailed polarization characteristics obtained in this work, further polarization compensation optimization can be carried out to improve the accuracy of fluorescence quantitative retrieval, thereby promoting the practical development of next-generation fluorescence remote sensing payloads.

**Author Contributions:** Conceptualization, Y.L. (Yiwei Li) and K.C.; Methodology, Y.L. (Yiwei Li) and Z.Z.; Formal analysis, K.C. and X.J.; Investigation, K.C. and X.J.; Data curation, Y.L. (Yiwei Li), X.F. and L.L.; Writing—original draft, Y.L. (Yiwei Li); Writing—review & editing, Y.L. (Yinnian Liu); Supervision, Y.L. (Yinnian Liu). All authors have read and agreed to the published version of the manuscript.

**Funding:** This research was funded by Advanced Research Project of Civil Aerospace Technologies: D040104 and National Natural Science Foundation of China: 42192582.

**Data Availability Statement:** The data presented in this study are available on request from the corresponding author due to the data are not publicly available due to privacy or ethical restrictions.

**Conflicts of Interest:** The authors declare no conflict of interest.

## References

1. Du, S.; Liu, L.; Liu, X.; Zhang, X.; Gao, X.; Wang, W. The Solar-Induced Chlorophyll Fluorescence Imaging Spectrometer (SIFIS) Onboard the First Terrestrial Ecosystem Carbon Inventory Satellite (TECIS-1): Specifications and Prospects. *Sensors* **2020**, *20*, 815. [CrossRef]
2. Coppo, P.; De Luca, E.; Nuzzi, D.; Gabrieli, R.; Paolino, P.; Bellomo, G.; Pekala, G.D. FLORIS: An Innovative Spectrometer for Fluorescence Measurement and Its Synergy with OLCI and SLSTR. *Eng. Proc.* **2023**, *51*, 48. [CrossRef]

3. Taccola, M.; Da Mota Silva, S.; Pereira do Carmo, J.; Petitjean, G.; Bock, R.; Fratacci, O.; Trastour, J.; Baroni, M.; Naldoni, S.; Nuzzi, D.; et al. FLEX Instrument: Status, Performances, and Lessons Learnt. In *Proceedings of the International Conference on Space Optics (ICSO 2022), Dubrovnik, Croatia, 3–7 October 2022*; SPIE: Bellingham, WA, USA, 2023; Volume 12777, p. 127770J. [CrossRef]
4. Moreno, J.F. The Fluorescence Explorer (FLEX) Mission: From Spectral Measurements to High-Level Science Products. In *Proceedings of the 2021 IEEE International Geoscience and Remote Sensing Symposium (IGARSS), Brussels, Belgium, 11–16 July 2021*; IEEE: New York, NY, USA, 2021; pp. 115–118. [CrossRef]
5. Moreno, J.F. The Fluorescence Explorer (FLEX): Mission Status and Data Exploitation Plans. In *2022 IEEE International Geoscience and Remote Sensing Symposium (IGARSS), Kuala Lumpur, Malaysia, 17–22 July 2022*; IEEE: New York, NY, USA, 2022; pp. 5015–5018. [CrossRef]
6. Nuzzi, D.; Pettinato, L.; Fossati, E.; Gabrieli, R.; Coppo, P.; Baroni, M.; De Luca, E.; Giunti, L.; Cavanna, A.; Romano, J.; et al. Improving Stray-Light Characterization beyond Blooming: The Experience of the FLORIS Optical Model Refurbished. In *Proceedings of the International Conference on Space Optics (ICSO 2022), Dubrovnik, Croatia, 3–7 October 2022*; SPIE: Bellingham, WA, USA, 2023; Volume 12777, p. 1277711. [CrossRef]
7. De Grave, C.; Verrelst, J.; Morcillo-Pallarés, P.; Pipia, L.; Rivera-Caicedo, J.P.; Amin, E.; Belda, S.; Moreno, J. Quantifying Vegetation Biophysical Variables from the Sentinel-3/FLEX Tandem Mission: Evaluation of the Synergy of OLCI and FLORIS Data Sources. *Remote Sens. Environ.* **2020**, *251*, 112101. [CrossRef] [PubMed]
8. Guanter, L.; Zhang, Y.G.; Jung, M.; Joiner, J.; Voigt, M.; Berry, J.A.; Frankenberg, C.; Huete, A.R.; Zarco-Tejada, P.; Lee, J.E.; et al. Global and Time-Resolved Monitoring of Crop Photosynthesis with Chlorophyll Fluorescence. *Proc. Natl. Acad. Sci. USA* **2014**, *111*, E1327–E1333. [CrossRef]
9. Zhang, Z.-Y.; Wang, S.-H.; Qiu, B.; Song, L.; Zhang, Y.-G. Retrieval of Sun-Induced Chlorophyll Fluorescence and Advancements in Carbon Cycle Application. *J. Remote Sens.* **2019**, *23*, 37–52. [CrossRef]
10. Meroni, M.; Rossini, M.; Guanter, L.; Alonso, L.; Rascher, U.; Colombo, R.; Moreno, J. Remote Sensing of Solar-Induced Chl-orophyll Fluorescence: Review of Methods and Applications. *Remote Sens. Environ.* **2009**, *113*, 2037–2051. [CrossRef]
11. Meroni, M.; Busetto, L.; Colombo, R.; Guanter, L.; Moreno, J.; Verhoef, W. Performance of Spectral Fitting Methods for Vegetation Fluorescence Quantification. *Remote Sens. Environ.* **2010**, *114*, 363–374. [CrossRef]
12. Alonso, L.; Gómez-Chova, L.; Vila-Francés, J.; Amoros-Lopez, J.; Guanter, L.; Calpe, J.; Moreno, J. Improved Fraunhofer Line Discrimination Method for Vegetation Fluorescence Quantification. *IEEE Geosci. Remote Sens. Lett.* **2008**, *5*, 620–624. [CrossRef]
13. Guanter, L.; Frankenberg, C.; Dudhia, A.; Lewis, P.E.; Gómez-Dans, J.; Kuze, A.; Suto, H.; Grainger, R.G. Retrieval and Gl-obal Assessment of Terrestrial Chlorophyll Fluorescence from GOSAT Space Measurements. *Remote Sens. Environ.* **2012**, *121*, 236–251. [CrossRef]
14. Perez-Priego, O.; Zarco-Tejada, P.J.; Miller, J.R.; Sepulcre-Canto, G.; Fereres, E. Detection of Water Stress in Orchard Trees with a High-Resolution Spectrometer through Chlorophyll Fluorescence in Filling of the $O_2$-A Band. *IEEE Trans. Geosci. Remote Sens.* **2005**, *43*, 2860–2869. [CrossRef]
15. Liu, X.; Liu, L. Improving Chlorophyll Fluorescence Retrieval Using Reflectance Reconstruction Based on Principal Components Analysis. *IEEE Geosci. Remote Sens. Lett.* **2015**, *12*, 1645–1649. [CrossRef]
16. Zhu, X.; Wang, B.; Xiong, Z.; Huang, Y. A Method to Eliminate the Zeroth Order with Low Polarization-Independent Loss by a Transmission Grating. *Optik* **2022**, *260*, 169049. [CrossRef]
17. Sierk, B.; Fernandez, V.; Bézy, J.-L.; Meijer, Y.; Durand, Y.; Courrèges-Lacoste, G.B.; Pachot, C.; Löscher, A.; Nett, H.; Te Hennepe, F. The Copernicus CO2M Mission for Monitoring Anthropogenic Carbon Dioxide Emissions from Space. *Proc. SPIE* **2021**, *11852*, 118523M. [CrossRef]
18. Li, H.; Peng, X.; Guan, C.; Hu, H. Progress in the Preparation and Characterization of Convex Blazed Gratings for Hyper-Spectral Imaging Spectrometer: A Review. *Micromachines* **2022**, *13*, 1689. [CrossRef]
19. Miles, D.M.; McCoy, J.; Grisé, F.; McEntaffer, R.L. Toward Blazed UV Gratings for the Habitable Worlds Observatory and Beyond. In *UV/Optical/IR Space Telescopes and Instruments: Innovative Technologies and Concepts XII*; SPIE: Bellingham, WA, USA, 2025; Volume 13623, pp. 302–312. [CrossRef]
20. Zeitner, U.D.; Dekker, H.; Burmeister, F.; Flügel-Paul, T.; Bianco, A.; Zanutta, A. High Efficiency Transmission Grating for the ESO CUBES UV Spectrograph. *Exp. Astron.* **2023**, *55*, 281–300. [CrossRef]
21. Kruczek, N.; Miles, D.M.; Fleming, B.; McEntaffer, R.; France, K.; Grisé, F.; McCandliss, S. High Efficiency Echelle Gratings for the Far Ultraviolet. *Appl. Opt.* **2022**, *61*, 8307–8317. [CrossRef]
22. Li, X.; Guo, X.; Li, Y.; Jia, Z.; Zhang, K.; Kong, F. Recent Progress of Interference Suppression Methods for Polarization Imaging Sensors. *Opt. Lasers Eng.* **2026**, *196*, 109398. [CrossRef]
23. Zhu, J.-C.; Shen, W.-M. Compact Anastigmatic Long-Slit Spectrometer. *J. Infrared Millim. Waves* **2019**, *38*, 542–548. [CrossRef]
24. Yu, T.-Y.; Qin, Y.; Jiang, L.; Duan, W.-B.; Liu, D.-Q. Design and Fabrication of an Ultra-Broadband Dichroic Beam-Splitter with Low Polarization. *J. Infrared Millim. Waves* **2024**, *43*, 408–414. [CrossRef]

25. Wu, Z.-K.; Shi, E.-T.; Wang, Y.-M.; Guo, B.-Z.; Li, P.-D. Design Method of Depolarizer in Converging Optical Path of Spectrometer. *Acta Opt. Sin.* **2022**, *42*, 53–60. [CrossRef]
26. Chen, H.-Y.; Chen, X.-H.; Pan, Q.; Zhu, J.-C.; Shen, W.-M. Design of Total Internal Reflection Immersed Gratings with High Diffraction Efficiency and Low Polarization Sensitivity. *Acta Opt. Sin.* **2023**, *43*, 80–87. [CrossRef]
27. Luo, H.-B.; Zhang, J.-C.; Gai, X.-Q.; Liu, Y. Development Status and Prospects of Polarization Imaging Technology (Invited). *Infrared Laser Eng.* **2022**, *51*, 109–118. [CrossRef]
28. Meister, G.; Kwiatkowska, E.J.; Franz, B.A.; Patt, F.S.; Feldman, G.C.; McClain, C.R. Moderate-Resolution Imaging Spectroradiometer Ocean Color Polarization Correction. *Appl. Opt.* **2005**, *44*, 5524–5535. [CrossRef] [PubMed]
29. Sun, J.-Q.; Xiong, X. MODIS Polarization-Sensitivity Analysis. *IEEE Trans. Geosci. Remote Sens.* **2007**, *45*, 2875–2885. [CrossRef]
30. Young, J.B.; Knight, E.; Merrow, C. MODIS Polarization Performance and Anomalous Four-Cycle Polarization Phenomenon. In *Earth Observing Systems III, San Diego, CA, USA, 19–21 July 1998*; SPIE: Bellingham, WA, USA, 1998; Volume 3439, pp. 94–103. [CrossRef]
31. Souaidia, N.; Moyer, D.; Meister, G.; Pellicori, S.; Waluschka, E.; Voss, K. MODIS Polarization Ray Tracing Analysis. In *Polarization Science and Remote Sensing II, San Diego, CA, USA, 2–4 August 2005*; SPIE: Bellingham, WA, USA, 2005; Volume 5888, p. 58880H. [CrossRef]
32. Pan, C.; Weng, F.; Flynn, L. Spectral Performance and Calibration of the Suomi NPP OMPS Nadir Profiler Sensor. *Earth Space Sci.* **2017**, *4*, 737–745. [CrossRef]
33. Otter, G.; Dijkhuizen, N.; Vosteen, A.; Brinkers, S.; Gür, B.; Kenter, P.; Sallusti, M.; Tomuta, D.; Veratti, R.; Cappani, A. On-Ground Re-Calibration of the GOME-2 Satellite Spectrometer Series. In *International Conference on Space Optics—ICSO 2012, Ajaccio, Corsica, France, 9–12 October 2012*; SPIE: Bellingham, WA, USA, 2017; Volume 10564, pp. 847–852. [CrossRef]
34. Wang, H.-B.; Hu, X.-Q.; Zhang, L.; Zhang, C.-B.; Ren, B.-C.; Huang, X.-X.; Wei, J. Polarization Correction for Grating Dispersive Imaging Spectrometer. *Acta Opt. Sin.* **2016**, *36*, 0812004. [CrossRef]
35. Yuan, Y.; Liu, Z.; Zheng, X.; Kang, Q.; Wu, H.; Li, J.; Li, S.; Luo, D.; Hong, J. Polarimetric Calibration of the Spaceborne Directional Polarimetric Camera Installed on the GF-5 Satellite. *Int. Arch. Photogramm. Remote Sens. Spat. Inf. Sci.* **2020**, *43*, 599–606. [CrossRef]
36. Tu, B.-H.; Hong, J.; Yao, P.-P.; Meng, B.-H.; Yuan, Y.-L.; Zhang, M.-M.; Weng, J.-W. Polarization Detection Performance of Directional Polarimetric Camera. *Acta Opt. Sin.* **2020**, *40*, 0712003. [CrossRef]
37. Stammes, P. Errors in UV Reflectivity and Albedo Calculations Due to Neglecting Polarization. In *SPIE's 1994 International Symposium on Optical Science, Engineering, and Instrumentation, San Diego, CA, USA, 24–29 July 1994*; SPIE: Bellingham, WA, USA, 1994; Volume 2311, pp. 227–235. [CrossRef]
38. Aben, I.; Helderman, F.; Stam, D.M.; Stammes, P. High-Spectral Resolution Polarisation Measurements of the Atmosphere with the GOME BBM. In *Optical Systems for Space and Defence, London, UK, 30 September–2 October 1997*; SPIE: Bellingham, WA, USA, 1997; Volume 3121, pp. 450–457. [CrossRef]
39. Waluschka, E.; Silverglate , P.R.; Ftaclas, C.; Turner, A.N. Polarization Sensitivity Analysis of an Earth Remote Sensing Instrument: The MODIS-N Phase B Study. In *Polarization Analysis and Measurement, San Diego, CA, USA, 19–24 July 1992*; SPIE: Bellingham, WA, USA, 1992; Volume 1746, pp. 96–103. [CrossRef]
40. Cui, C.-G.; An, N.; Yu, Z.-W.; Zhang, S.-J.; Wang, W.-G.; Xu, P.-M. Suppression and Measurement of Polarization Response of th-e Solar-Induced Chlorophyll Fluorescence Imaging Spectrometer (SIFIS). *Spacecr. Recovery Remote Sens.* **2022**, *43*, 85–96. [CrossRef]
41. Coppo, P.; Pettinato, L.; Nuzzi, D.; Fossati, E.; Taiti, A.; Gabrieli, R.; Campa, A.; Taccola, M.; Bézy, J.-L.; Francois, M. Instrument Predevelopment Activities for FLEX Mission. *Opt. Eng.* **2019**, *58*, 075102. [CrossRef]
42. Coppo, P.; Taiti, A.; Pettinato, L.; Francois, M.; Taccola, M.; Drusch, M. Fluorescence Imaging Spectrometer (FLORIS) for ESA FLEX Mission. *Remote Sens.* **2017**, *9*, 649. [CrossRef]
43. Zhang, Z.; Fu, A.; Xu, J.; Lin, J.; Zhang, X.; Zhang, Y. First global retrievals of solar induced chlorophyll fluorescence from the SIFIS instrument onboard the Chinese goumang satellite. *Geophys. Res. Lett.* **2025**, *52*, e2025GL118327. [CrossRef]
44. Zhang, Z.C.; Liu, Y.N.; Cao, K.Q.; Li, Y.W.; Ke, Y.L.; Jia, X.W.; Chen, Q.; Feng, X.F.; Liu, X.B.; Zhou, W.Y.N.; et al. A Spaceborne Sun-Induced Chlorophyll Fluorescence Spectral Detection and Imaging System. China Invention Patent CN 202510717743.9, 8 August 2025.
45. Yan, L.; Li, Y.; Chandrasekar, V.; Mortimer, H.; Peltoniemi, J.; Lin, Y. General Review of Optical Polarization Remote Sensing. *Int. J. Remote Sens.* **2020**, *41*, 4853–4864. [CrossRef]
46. Knight, E.J. Effect of Polarization on the Application of Radiometric Calibration Coefficients to Infrared Earth Scenes. In *Earth Observing System, Denver, CO, USA, 4–9 August 1996*; SPIE: Bellingham, WA, USA, 1996; Volume 2815, pp. 84–95. [CrossRef]
47. Chipman, R.A.; Lam, W.-S.T.; Young, G. *Polarized Light and Optical Systems*; Hou, J.; Zhang, X.; Wang, D., Translators; Tsinghua University Press: Beijing, China, 2023; Volume 2.

48. Tilstra, L.G.; Schutgens, N.A.J.; Stammes, P. *Analytical Calculation of Stokes Parameters Q and U of Atmospheric Radiation*; WR-03-01; KNMI: De Bilt, The Netherlands, 2003; pp. 1–13.
49. Li, H.; Li, Z.; Huang, Y.; Lin, G.; Zeng, J.; Li, H.; Wang, S.; Han, W. Analysis and Correction of Polarization Response Calibration Error of Limb Atmosphere Ultraviolet Hyperspectral Detector. *Sensors* **2022**, *22*, 8542. [CrossRef]

**Disclaimer/Publisher's Note:** The statements, opinions and data contained in all publications are solely those of the individual author(s) and contributor(s) and not of MDPI and/or the editor(s). MDPI and/or the editor(s) disclaim responsibility for any injury to people or property resulting from any ideas, methods, instructions or products referred to in the content.